frontiers | Frontiers in Materials

TYPE Original Research
PUBLISHED 19 April 2024
DOI 10.3389/fmats.2024.1390421

OPEN ACCESS

EDITED BY
Chenxi Zhai,
Cornell University, United States

REVIEWED BY
Shengjian Qin,
Shijiazhuang Tiedao University, China
Bowen Huang,
Hunan University, China

*CORRESPONDENCE
Guangtian Zhang,
syzx1206@163.com

RECEIVED 23 February 2024
ACCEPTED 28 March 2024
PUBLISHED 19 April 2024

CITATION
Fu S, Li Z, Zhang G, Zhang B and Zhang Y (2024), Study on characteristics of ammonia alkali white mud and mechanical properties of preparation of fluid solidified soil. *Front. Mater.* 11:1390421. doi: 10.3389/fmats.2024.1390421

Study on characteristics of ammonia alkali white mud and mechanical properties of preparation of fluid solidified soil

Shifeng Fu[1,2], Zhiquan Li[3,4], Guangtian Zhang[1,2]*, Biao Zhang[3,4] and Yanjia Zhang[1,2]

[1]Hebei Provincial Institute of Building Science and Technology Co., Ltd., Shijiazhuang, China, [2]Hebei Province Science and Technology Key Laboratory of Solid Waste for Building Materials, Shijiazhuang, China, [3]Tangshan Sanyou Chemical Co., Ltd., Tangshan, China, [4]Hebei Province Soda Ash Reduction and Resource Utilization Technology Innovation Center, Tangshan, China

To address the challenges posed by the significant quantity of ammonia-alkali white mud, this study explores the preparation of fluid solidified soil using ammonia-alkali white mud, mineral powder, and fly ash. The findings reveal that ammonia-alkali white mud primarily comprises sulfate, carbonate, and soluble chloride salt, with an alkaline solution and a well-developed pore structure. Optimal fluid solidified soil formulation, comprising 30% white mud, 30% salt mud, 25% mineral powder, 10% fly ash, and 5% calcium oxide, yields a slurry fluidity of 176 mm and a compressive strength of 3.98 MPa at 28 days. Microscopic analysis highlights AFt and C-S-H gel as the principal hydration products of fluid solidified soil. The fine particles of calcium carbonate in ammonia-alkali white mud fill the structural pores and intertwine with the hydration products, facilitating the formation of a dense structure, which constitutes the primary source of strength in fluid solidified soil. Furthermore, the heavy metal content of the solidified soil aligns with the first type of land use requirements outlined in the GB 36600-2018 standard, and the toxicity of the leaching solution adheres to the emission concentration limit stipulated by GB 8978-1996.

KEYWORDS

ammonia alkali white mud, fluid solidified soil, working performance, mechanical property, hydration products, leaching toxicity

1 Introduction

Soda ash is an essential chemical material in driving national economies forward. The widespread adoption of the ammonia-alkali process in large-scale industrial soda ash production has notably contributed to this. However, a consequential byproduct of this method is ammonia-alkali white mud, a solid waste (Liu, 2021). Shockingly, for every ton of soda ash produced, approximately 300–600 kg of solid waste is discharged (Zhao et al., 2019), resulting in an annual accumulation of over seven million tons of ammonia-alkali white mud in China alone (Liao et al., 2012; Wang et al., 2020). Sadly, due to the lack of technically and economically feasible utilization methods, these resources have remained largely untapped. Currently, the only recourse is containment through dams, posing significant challenges to ammonia-alkali enterprises in terms of

resource management, safety, environmental impact, and economic burden. Ammonia-alkali white mud primarily comprises calcium carbonate, calcium sulfate, silica, soluble salts, and is characterized by its alkaline nature (Chen et al., 2022). Notably, it lacks heavy metals and polluting organic matter (Chen et al., 2022). Current utilization efforts mainly involve its incorporation into cement (Xu et al., 2021), mortar (Zhang et al., 2017), carbonized brick (Zhao et al., 2017), soil conditioning (Pan and Xu, 2017), cementitious materials and concrete (Xu et al., 2020), engineering soil (Gong et al., 2023), and as a component in flue gas desulfurization and adsorption (Peng and Liu, 1999; Rui et al., 2006). However, these methods have limitations in scale and efficiency, necessitating a comprehensive expansion of ammonia-alkali white mud utilization.

Fluid solidified soil, a novel filling material, presents itself as a promising solution. It involves mixing base and cementing materials with water, offering advantages such as low cost, excellent construction performance, and uniform slurry consistency. Its application spans various domains, including pipe gallery foundation trenching, deep foundation pit backfilling, goaf backfilling, pavement sub-basing, and more (Du et al., 2021; He, 2023; Wang et al., 2023; Ye, 2023; Zhnag et al., 2023; Su et al., 2024). Typically, the base material consists of low-grade, non-standard materials, including engineering waste soil, industrial residues, and engineering mud (Zhou et al., 2024). Notably, ammonia-alkali white mud shares similar physical and mechanical properties with natural soil, rendering it a potential candidate for base material in fluid solidified soil development (Yan, 2008). Traditionally, cement serves as the binder in fluid solidified soil, contributing to pollution and high carbon emissions. However, advancements have introduced alternatives such as slag and fly ash, derived from industrial solid waste, to replace cement (Bao et al., 2023; Zhong et al., 2023). Given the alkaline nature and sulfate/chloride composition of ammonia-alkali white mud, it can serve as an active activator for slag and fly ash. Hence, this study endeavors to use ammonia-alkali white mud, slag, and fly ash as primary raw materials for preparing liquid solidified soil. It aims to investigate the influence of white mud and salt mud quantities on the working performance and mechanical properties of liquid solidified soil. Furthermore, the hydration mechanism of ammonia-alkali white mud-based liquid solidified soil will be scrutinized through various microscopic analysis methods. Ultimately, this research aims to present an effective strategy for broadening the comprehensive utilization of ammonia-alkali white mud.

2 Materials and methods

2.1 Raw materials

The ammonia alkali white mud (AAWD) and fly ash (FA) utilized in this study were sourced from Tangshan Sanyou Chemical Co., Ltd., while the ground slag (GS) was obtained from Hebei Jingye Group. Calcium oxide served as a pure reagent for chemical analysis. Table 1 presents the chemical composition of both slag and fly ash.

2.1.1 Ammonia-alkali white mud

The AAWD employed in this investigation encompasses both salt mud (SM) and white mud (WM), constituting the solid waste generated during the ammonia-alkali soda ash production process. White mud originates from the solid waste produced during the ammonia evaporation phase of alkali mother liquor's lime milk. Salt mud predominantly arises from solid waste generated during raw salt dissolution and lime milk-glauber or soda refining brine processes.

2.1.2 Ground slag

The ground slag utilized in this experiment is a molten material primarily composed of silicate or aluminosilicate, a byproduct of the blast furnace's pig iron smelting process. It has been ground to a specific surface area of 453 m^2/kg using a vertical mill, with activity indexes of 85% and 104% at 7 and 28 days, respectively. Figure 1 shows the particle size analysis of granulated blast furnace slag powder. The characteristic particle sizes of ground slag are d_{10} = 2.822 μm, d_{50} = 10.893 μm, and d_{90} = 29.131 μm, respectively.

2.1.3 Fly ash

The fly ash employed herein is fine ash collected from flue gas post-coal-fired power generation. It possesses a water demand ratio of 100%, with activity indexes of 61% and 73% at 7 and 28 days, respectively. Figure 1 shows the particle size analysis of fly ash. The characteristic particle size distribution of fly ash is d_{10} = 4.800 μm, d_{50} = 29.226 μm, and d_{90} = 92.412 μm.

2.1.4 CaO

The CaO utilized in the experiment is a chemically pure reagent sourced from the Hongyan Reagent Factory in Hedong District, Tianjin.

TABLE 1 Chemical composition of raw materials.

Material	Mass fraction *w*/%										
	SiO_2	CaO	MgO	Al_2O_3	Fe_2O_3	SO_3	Na_2O	K_2O	MnO	TiO_2	P_2O_5
FA	52.10	4.27	0.84	35.30	2.92	0.77	0.33	1.18	-	1.02	0.38
GS	29.09	42.32	8.68	13.27	0.56	1.91	0.48	0.49	1.20	1.66	-

TABLE 2 Mix ratio of fluid solidified soil.

Number	GS/%	FA/%	WM/%	SM/%	CaO/%
A-1	25	10	60	0	5
A-2	25	10	50	10	5
A-3	25	10	40	20	5
A-4	25	10	30	30	5
A-5	25	10	20	40	5
A-6	25	10	10	50	5
A-7	25	10	0	60	5

2.2 Test ratio

The flow solidified soil was formulated through the consolidation of mineral powder and fly ash with ammonia alkali white mud. The composition was standardized with slag powder and fly ash constituting 35%, ammonia alkali white mud comprising 60%, and maintaining a water-solid ratio of 0.7. Table 2 illustrates the specific test ratios in terms of mass ratios.

2.3 Experiment methods

Particle Size Analysis and Material Properties Measurement: Particle size analysis of white mud, salt mud, ground slag, and fly ash was conducted using the LS-909 laser particle size analyzer. Material moisture detection followed the guidelines outlined in GB/T 6284-2006'General Method for Determination of Moisture in Chemical Products,' while material density detection adhered to GB/T 208-2014'Cement Density Determination Method'.

Fluidity Test: The fluidity test was executed in accordance with the Japanese Road Engineering Group JHSA 313-1992'Test Method of Air-Entraining Mortar and Air-Entraining Mortar'. The stirred slurry was poured into a cylindrical cylinder measuring 80 mm in inner diameter and 80 mm in height, placed on a smooth hard plastic plate. Gently tapping the outer side of the cylinder facilitated the slurry's even distribution. Subsequently, the sample was carefully leveled using a flat knife, and the hollow cylinder was slowly lifted to allow the sample to flow naturally. After 1 min, diameters in two vertical directions were measured, and the average value was recorded as the fluidity of the fluid-solidified soil.

Compressive Strength Test: The compressive strength test method followed T/CECS 1175-2022'Technical Specification for Filling Self-Compacting Solidified Soil'. Test molds measuring 70.7 mm × 70.7 mm × 70.7 mm were used, and after standard curing for 24 h, the mold was removed. The test block underwent further curing to the specified age before undergoing the compressive strength test.

Material Analysis: Chemical composition analysis was performed using X-ray fluorescence spectrometry (XRF), while phase composition analysis utilized X-ray diffraction analyzer (XRD). The microstructure of the material was examined via field emission scanning electron microscope (SEM), and thermal properties were analyzed through thermogravimetric differential scanning calorimetry (TG-DSC).

Leaching Toxicity and Heavy Metal Content: Leaching toxicity and heavy metal content were determined following the protocols outlined in HJ/T 299-2007, HJ 751-2015, HJ 786-2016, HJ 749-2015, GB 5085.3-2007 (Appendix E: Determination of Arsenic, Antimony, Bismuth, and Selenium in Solid Waste), and GB/T 15555.1-1995. The concentrations of heavy metals in the solution were also assessed.

These comprehensive analyses provide crucial insights into the physical, mechanical, and chemical properties of the solidified soil, ensuring a thorough understanding of its characteristics and potential environmental impact.

3 Experimental results and analysis

3.1 Source and physicochemical properties of ammonia alkali white mud

3.1.1 Source of ammonia alkali white mud

The production of soda ash through the ammonia alkali method involves an intricate inorganic chemical process. Key raw materials include raw salt, limestone, and coke. The production journey primarily comprises limestone calcination and lime milk preparation, brine preparation and purification, ammoniation of refined brine, carbonation of ammonia brine, filtration, sodium bicarbonate calcination, and ammonia recovery. Salt mud, a byproduct of the brine preparation and purification phase, originates from the removal of calcium and magnesium impurity ions in crude salt. This purification process, achieved through lime milk-glauber or soda ash methods, results in the formation of solid waste, including calcium and magnesium insoluble salts, which constitute salt mud. The principal reactions involved are as follows:

$$Mg^{2+} + Ca(OH)_2 \rightarrow Mg(OH)_2 + Ca^{2+}$$

$$Ca^{2+} + Na_2CO_3 \rightarrow CaCO_3 + 2Na^+$$

$$Ca^{2+} + Na_2SO_4 \rightarrow CaSO_4 + 2Na^+$$

The white mud is derived from the lime milk ammonia evaporation process of the alkali mother liquor. This involves mixing lime milk with the mother liquor, leading to the conversion of combined ammonia in the mother liquor into free ammonia. During the ammonia recovery process, which entails heating and distillation in the ammonia distillation tower, white mud is generated as a solid waste. The primary reactions involved are as follows:

$$2NH_4Cl + Ca(OH)_2 \rightarrow 2NH_3 + CaCl_2 + 2H_2O$$

$$(NH_4)_2SO_4 + Ca(OH)_2 \rightarrow 2NH_3 + CaSO_4 + 2H_2O$$

$$(NH_4)_2CO_3 + Ca(OH)_2 \rightarrow 2NH_3 + CaCO_3 + 2H_2O$$

$$Na_2(SO_4) + CaCl_2 \rightarrow CaSO_4 + 2NaCl$$

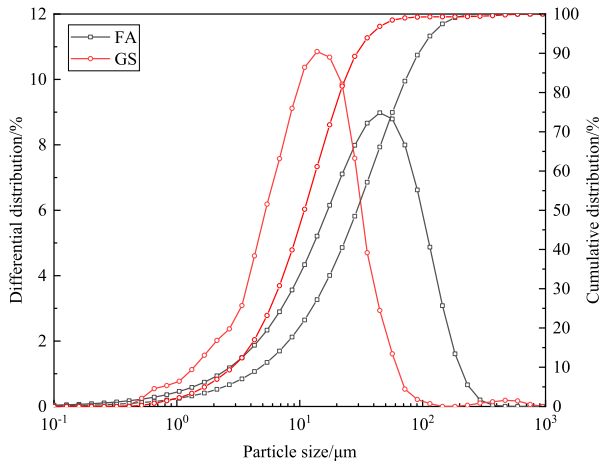

FIGURE 1
Particle size distribution of fly ash and ground slag.

From the production process of ammonia alkali white mud, it is evident that this substance primarily consists of carbonate, sulfate, soluble chloride salts, and other compounds. Additionally, its aqueous solution exhibits a weakly alkaline nature.

3.1.2 Physicochemical properties of ammonia-alkali white mud

The moisture content of salt mud and white mud was measured at 49.2% and 55.3%, respectively, and their respective densities were recorded as 2.25 g/cm^3 and 1.84 g/cm^3. Figure 2A illustrates the particle size analysis results of white mud and salt mud. Notably, the characteristic particle size of salt mud is reported as d_{10} = 5.379 μm, d_{50} = 22.660 μm, and d_{90} = 56.661 μm. Conversely, the characteristic particle size of white mud is d_{10} = 4.515 μm, d_{50} = 14.260 μm, and d_{90} = 29.677 μm, indicating a finer particle size compared to salt mud.

Table 3 presents the chemical composition of ammonia alkali white mud. Analysis reveals that salt mud predominantly comprises calcium, magnesium, sulfur, and other elements, with the combined content of these three elements nearing 90%. Conversely, white mud is primarily composed of calcium, chlorine, magnesium, silicon, sulfur, and other elements, with calcium representing 46.20% of its composition. Notably, the chloride content in salt mud and white mud is reported as 3.51% and 16.50%, respectively, indicating a notably higher chloride ion concentration in white mud.

Figure 2B shows the XRD pattern of salt mud and white mud. Table 4 provides the quantitative analysis of salt mud and white mud. The predominant mineral phases identified in salt mud encompass dihydrate gypsum ($CaSO_4{\cdot}2H_2O$), hemihydrate gypsum ($CaSO_4{\cdot}0.5H_2O$), brucite ($Mg(OH)_2$), and calcite ($CaCO_3$). Notably, gypsum constitutes the majority, accounting for up to 80.9% of the composition, while calcite and brucite phases collectively represent 6–7% of the total content. Additionally, small quantities of halite, quartz, and rutile phases were detected. Conversely, white mud comprises main mineral phases such as halite ($CaCl_2$, NaCl), calcite ($CaCO_3$), and hemihydrate gypsum ($CaSO_4{\cdot}0.5H_2O$). Here, the gypsum phase constitutes 36.1% of the composition, with the halite phase comprising 20.1%, and calcite contributing 38.3%.

Figures 2C, D presents scanning electron microscope (SEM) images of both salt mud and white mud. Notably, salt mud particles appear coarser compared to white mud, exhibiting angular shapes and an uneven distribution. In contrast, white mud features a higher concentration of fine particles, resulting in a larger specific surface area. These fine particles tend to stack together, forming a honeycomb-like structure with a well-developed pore network. This distinctive morphology contributes to the higher water content observed in white mud compared to salt mud.

3.2 Working performance and mechanical properties of flow solidified soil

3.2.1 Working performance

Figure 3A shows the results of the fluidity test conducted on the flow solidified soil. It is evident from the figure that as the content of salt mud increases, the fluidity of the solidified soil gradually improves. Specifically, compared to the fluidity of the A-1 group at 138 mm, the fluidity of the A-2~7 groups increases by 5.1%, 13.8%, 27.5%, 34.1%, 37.7%, and 40.4%, respectively. This observed trend can be attributed to several factors. Firstly, the finer particle size and larger specific surface area of white mud particles (with a d_{90} of 29.677 μm) compared to salt mud particles (with a d_{90} of 56.661 μm) contribute to enhanced fluidity. Moreover, the more developed pore structure of white mud results in stronger water absorption capabilities compared to salt mud, consequently reducing the fluidity of solidified soil comprised solely of white mud. However, with the addition of salt mud, the relative proportion of white mud decreases, leading to reduced water demand within the system and subsequent improvement in fluidity. Furthermore, the inclusion of salt mud enhances the particle size distribution of the fluid solidified soil system, further contributing to increased fluidity. Nevertheless, as the content of salt mud increases significantly, coarse particles become more prevalent in the solidified soil, leading to a deterioration in particle gradation and a gradual slowdown in the rate of fluidity improvement. Ultimately, when the mass ratio of white mud to salt mud reaches 1:1, the fluidity of the solidified soil reaches 176 mm, meeting the technical requirements for flow filling.

3.2.2 Mechanical properties

Figure 3B presents the compressive strength of flow solidified soil at different ages. It reveals that as the content of white mud decreases and the content of salt mud increases, the compressive strength of the fluid solidified soil initially rises and then declines at 3, 7, and 28 days. Furthermore, the compressive strength of the solidified soil test blocks increases with the duration of curing. At the 3-day mark, the compressive strength of the fluid solidified soil ranges from 0.21 to 1.25 MPa, with the highest value observed in the A-2 group with a white mud to salt mud ratio of 5:1, reaching 1.25 MPa. Subsequently, at 7 days and 28 days, the compressive strength ranges from 0.63 to 3.38 MPa and 1.23–3.98 MPa, respectively. Notably, when the mass ratio of white mud to salt mud is 1:1, the fluid solidified soil exhibits the maximum compressive strength, reaching 3.38 MPa and 3.98 MPa at 7 and 28 days, respectively.

The compressive strength results indicate that the fluid solidified soil outperforms both single white mud or salt mud groups

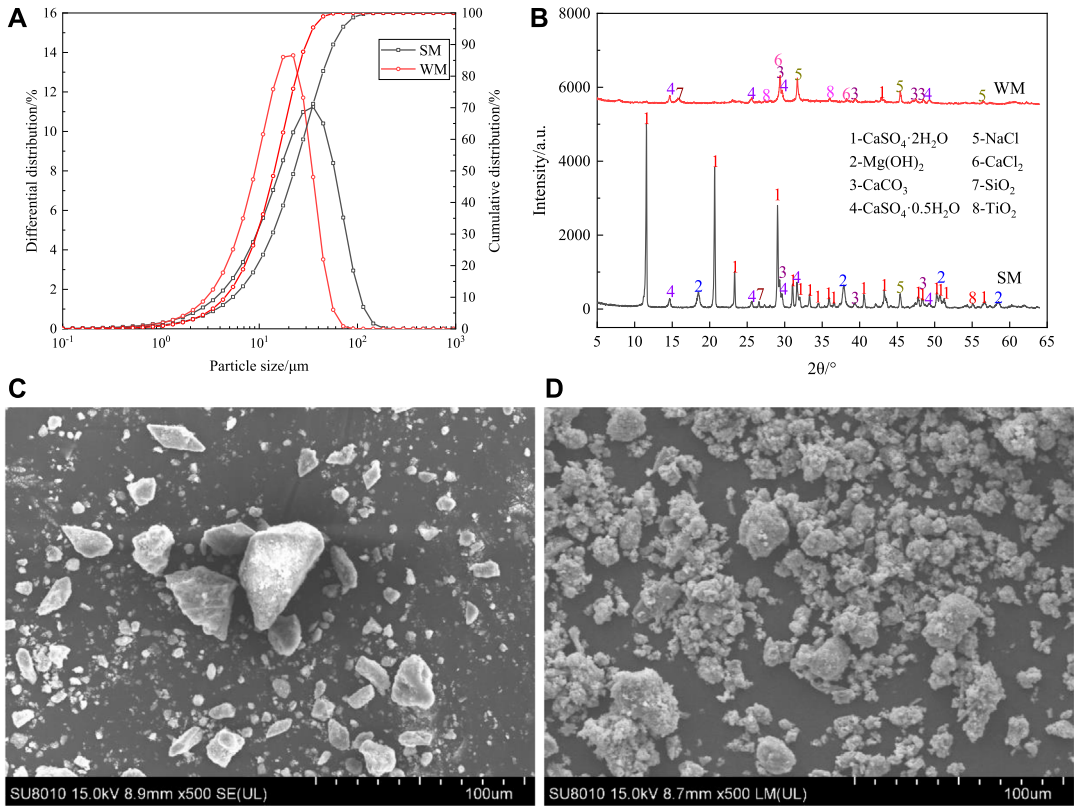

FIGURE 2
(A) Particle size distribution of white mud and salt mud, **(B)** XRD patterns of salt mud and white mud, **(C)** SEM images of salt mud, **(D)** SEM images of white mud.

TABLE 3 Chemical composition of ammonia alkali white mud.

Material	Mass fraction *w*/%								
	CaO	MgO	Al_2O_3	SiO_2	SO_3	Na_2O	K_2O	Fe_2O_3	Cl
SM	30.90	27.80	0.74	2.99	30.20	3.08	0.18	0.27	3.51
WM	46.20	10.10	3.02	10.90	10.50	1.30	0.35	0.84	16.50

TABLE 4 XRD phase quantitative analysis of white mud and salt mud.

Material	Mass fraction *w*/%						
	$CaSO_4·2H_2O$	$Mg(OH)_2$	$CaCl_2$、NaCl	$CaSO_4·0.5H_2O$	$CaCO_3$	SiO_2	TiO_2
SM	74.2	6.3	2.7	8.7	6.7	0.7	0.7
WM	4.9	-	20.1	31.2	38.3	1.8	3.7

when mixed. This is attributed to the depolymerization and polymerization of active Si-O and Al-O bonds in slag and fly ash in an alkaline environment. These reactions, along with the presence of gypsum phase and chloride salt, facilitate the formation of ettringite (AFt), C-S-H gel, and riedel salt, thus contributing to the strength of the hardened paste. Furthermore, the phase analysis indicates a higher content of gypsum phase in salt mud compared to white mud. Consequently, as the content of salt mud increases in the white mud and salt mud mixture, the gypsum phase content rises gradually, promoting the formation of ettringite and enhancing the solidified soil's strength. Additionally, the mixing of white mud and salt mud with varying particle sizes optimizes the particle gradation of the solidified soil slurry, improving its compactness and further boosting strength. However, an optimal proportion of 1:1 for salt

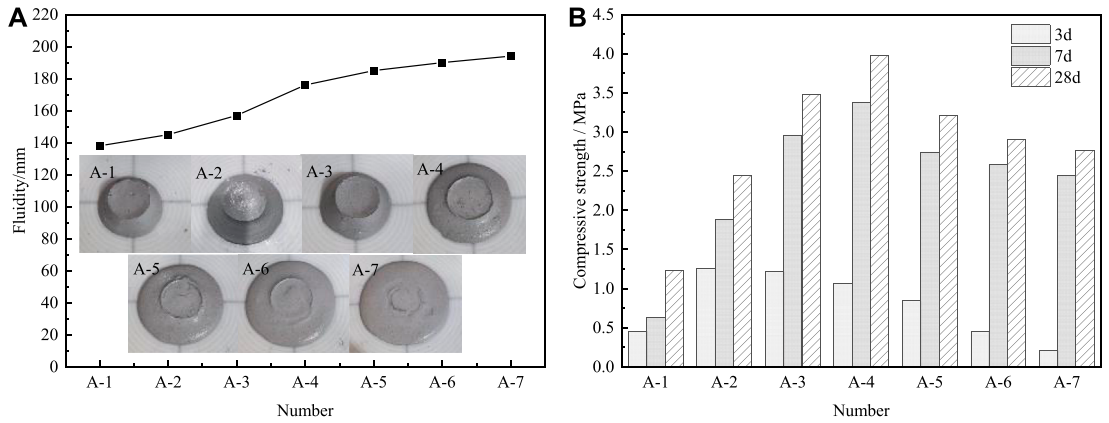

FIGURE 3
(A) Flow test results, **(B)** Compressive strength test results.

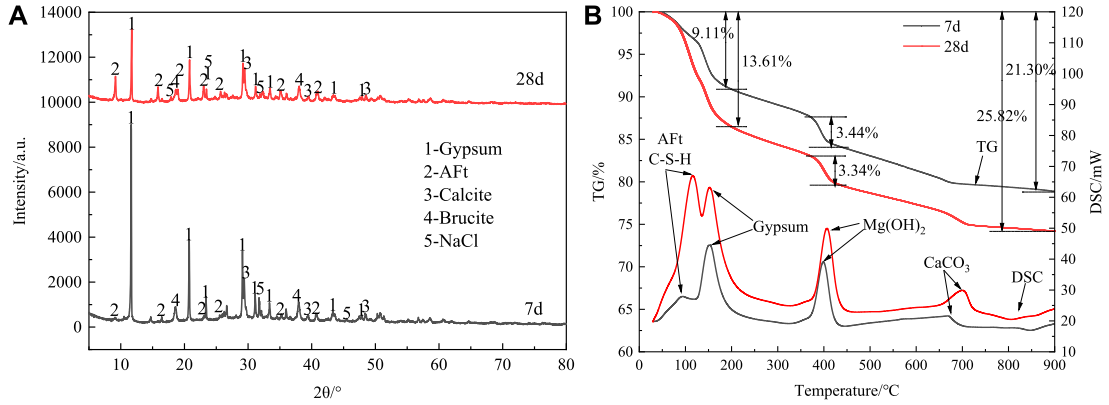

FIGURE 4
(A) XRD patterns of sclerotic body at different ages, **(B)** TG-DSC curves of sclerotic body at different ages.

mud to white mud is observed. Beyond this ratio, the compressive strength of the solidified soil diminishes.

3.3 Hydration products of fluid solidified soil

3.3.1 X-ray diffraction analysis

Figure 4A shows the XRD patterns of the A-4 group hardened body at 7 and 28 days of age. Upon examination of Figure 4A, it becomes apparent that after 7 days of curing, the diffraction peaks corresponding to gypsum, AFt, calcium carbonate, NaCl (halite), and brucite phases predominate in the hardened body. Additionally, distinct convex hulls emerge within the 25°–35° range, indicative of a non-crystalline structure characteristic of the hydration product C-S-H gel (Zhang et al., 2022). The physical and chemical properties analysis of salt mud and white mud reveals that phases such as gypsum, calcium carbonate, sodium chloride, and brucite are introduced into the hardened body by these materials. Meanwhile, the AFt phase and C-S-H gel are generated through the synergistic hydration reaction of ammonia-alkali white mud, slag, and fly ash, serving as the primary sources of strength for the hardened body (Du et al., 2022). Following 28 days of curing, no new diffraction peaks emerge in the XRD pattern of the hardened body, indicating stability in the phase composition over time. However, in comparison with the 7-day XRD pattern, the intensity of the gypsum phase diffraction peaks diminishes, while that of the AFt phase intensifies. This suggests that gypsum in the ammonia-alkali white mud actively participates in the hydration reaction, reacting with mineral powder and fly ash to produce more AFt and C-S-H gel. Consequently, the macroscopic strength of the solidified soil test block is further enhanced. The intensity of the diffraction peaks corresponding to calcium carbonate and brucite remains relatively unchanged across different ages, indicating a lower degree of participation in the hydration reaction for these phases.

3.3.2 Thermogravimetric differential scanning calorimetry analysis

Figure 4B shows the TG-DSC curves of the A-4 hardened body at 7 and 28 days. Analysis of the curves reveals four distinct endothermic peaks within the 30°C–900°C temperature range. The two endothermic peaks observed below 200°C primarily arise from

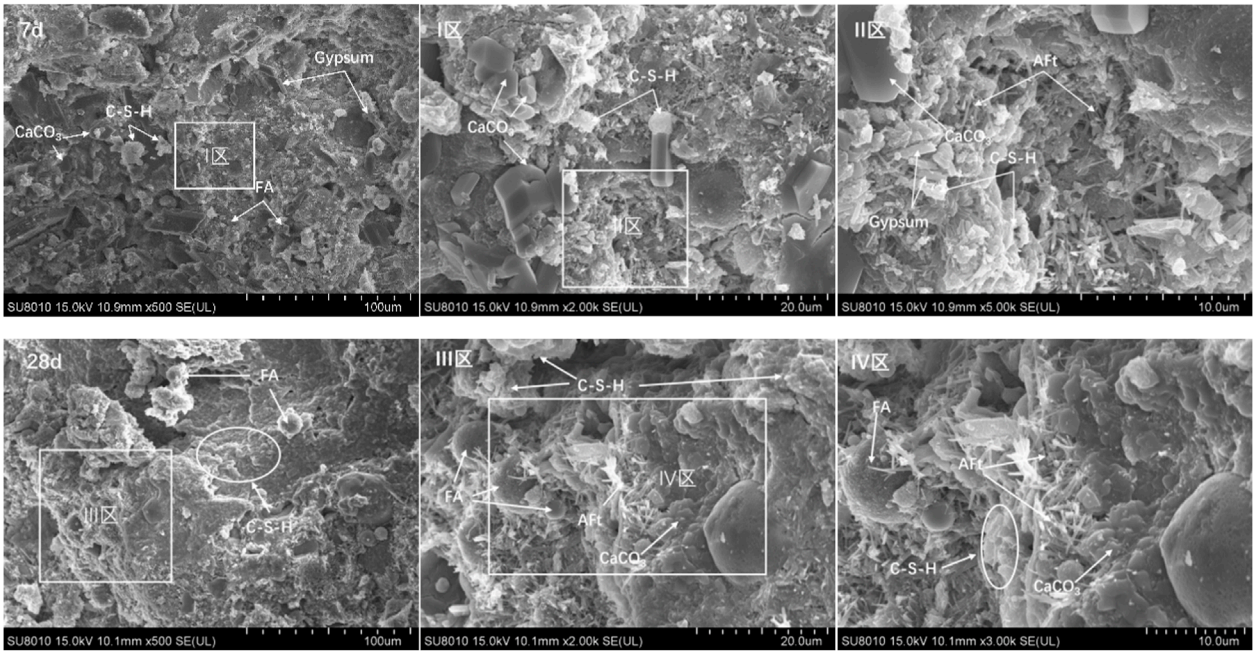

FIGURE 5
SEM morphology of hardened body at 7 and 28 days.

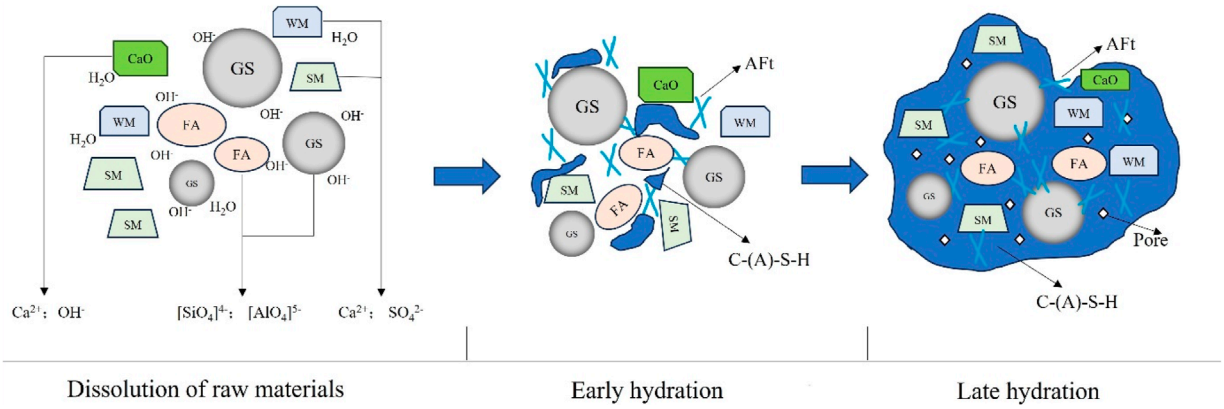

FIGURE 6
Schematic of hydration process of solidified soil.

the dehydration of hydration products such as AFt, C-S-H gel, and gypsum (Sun et al., 2022; Zhu et al., 2023). This inference aligns with the mineral composition of the raw materials and XRD analysis results. Furthermore, the endothermic peak occurring around 360°C–430°C is attributed to the presence of brucite introduced by ammonia-alkali white mud. Additionally, the weight loss observed near 700°C stems from the decomposition of calcium carbonate, another constituent introduced by ammonia-alkali white mud.

Due to the variance in the temperature ranges of weight loss for different substances, the weight loss within distinct temperature intervals can serve as a means to characterize the mass fraction of each substance. As depicted by the TG curve, at the 7-day mark, the weight loss rates were recorded as 9.11% at 200°C, 3.44% within the range of 360°C–430°C, and 21.30% at 900°C. This indicates significant mass loss associated with dehydration and decomposition processes within these temperature ranges. Upon reaching 28 days of curing, owing to the ongoing hydration reaction, hydration products such as AFt and C-S-H gel continued to form, resulting in a 4.50% increase in the weight loss rate at 200°C. Conversely, the weight loss rate remained relatively stable within the range of 360°C–430°C, suggesting minimal involvement of brucite in the hydration reaction. Furthermore, the total weight loss rate increased by 4.52% at 900°C after 28 days, a change consistent with the increase observed at 200°C. This suggests that calcium carbonate did not partake in the hydration reaction, corroborating the findings of the XRD analysis.

TABLE 5 Heavy metal content in solidified soil.

Sample	mg/kg						
	Arsenic	Cadmium	Hexavalent chromium	Copper	Mercury	Nickel	Lead
Solidified soil	11.30	0.36	ND	43.00	0.26	22.00	46.00
The first type of land	20	20	3.0	2000	8	150	400
The second type of land	60	65	5.7	18000	800	38	900

Note: ND, is not detected.

TABLE 6 Heavy metal leaching toxicity of solidified soil.

Sample	Arsenic	Cadmium	Hexavalent chromium	Total chromium	Copper	Mercury	Nickel	Lead
Solidified soil	0.49 μg/L	ND	ND	0.46 μg/L	0.18 μg/L	ND	ND	ND
GB 8978-1996	0.5 mg/L	0.1 mg/L	0.5 mg/L	1.5 mg/L	0.5 mg/L	0.05 mg/L	1.0 mg/L	1.0 mg/L

Note: ND, is not detected.

3.3.3 Scanning electron microscope analysis

To delve deeper into the factors contributing to the strength development of the fluid solidified soil, microscopic analysis was conducted on the A-4 group test blocks exhibiting favorable fluidity and compressive strength characteristics. Figure 5 presents scanning electron microscope images of the A-4 group test blocks at 7 and 28 days of age. An abundance of calcium carbonate particles, flocculent C-S-H gel, needle-like ettringite crystals, fly ash, and gypsum are clearly visible. At the 7-day mark, calcium carbonate particles act as both a skeleton and nucleation matrix, facilitating the formation of C-S-H gel on their surfaces. Simultaneously, overlapping needle-like ettringite crystals serve as a structural framework. However, due to relatively limited hydration product formation at this stage, the overall structure appears loose, resulting in comparatively lower strength. By the 28-day mark, numerous fly ash particles undergo depolymerization, leading to the appearance of flocculent gel products on their surfaces. Additionally, the hydration reaction persists, with a proliferation of C-S-H gels filling the pores formed by ettringite and calcium carbonate. Consequently, the hydration products become more intricately intertwined and interlocked, optimizing the pore structure and increasing the compactness of the hardened body. As a result, the strength of the fluid solidified soil experiences further enhancement.

3.3.4 Mechanism analysis

Through the analysis of hydration products, the hydration process, and the microstructure of solidified soil, the hydration process can be delineated into three distinct stages: dissolution of raw materials, rapid formation of hydration products, and the formation of a dense structure. Figure 6 shows the hydration diagram of solidified soil at these different stages.

In the early hydration stage, the dissolution reaction of raw materials predominates. Blast furnace slag and fly ash possess a silicate network-like vitreous structure, which is initially resistant to water but becomes disrupted in an alkaline environment. CaO in the raw material reacts with water to yield calcium hydroxide (Eq. 1), thereby augmenting the solution's alkalinity. Concurrently, the active silicon and aluminum present in the slag and fly ash undergo depolymerization in the alkaline milieu engendered by the hydration of calcium oxide. This process liberates active SiO_2 and AlO_2^- ions, fostering the formation of $[H_3SiO_4]^-$ tetrahedrons, $[H_3AlO_4]^{2-}$ tetrahedrons, and $[Al(OH)_6]^{3-}$ octahedrons (Eqs 2–4). Moreover, the gypsum in white mud and salt mud dissolves in water, yielding abundant Ca^{2+} and SO_4^{2-} ions (Eq. 5). In the alkaline environment, $[Al(OH)_6]^{3-}$ rapidly reacts with the aqueous Ca^{2+} and SO_4^{2-} to generate AFt (Eq. 6). Meanwhile, $[H_3SiO_4]^-$ tetrahedrons and $[H_3AlO_4]^{2-}$ ions can re-polymerize with Ca^{2+} in the solution, forming C-S-H and C-A-H gels (Eq. 7). These processes collectively contribute to the early strength development of the solidified soil. In the subsequent hydration stages, as fly ash and mineral powder continue to dissolve, the production of C-S-H gel and AFt persists. Consequently, the pores within the hardened slurry are continuously filled, resulting in densification of the structure and enhancement of its integrity. This densification ultimately contributes to the strength improvement in the later stages of the solidified soil.

$$CaO + H_2O \rightarrow Ca^{2+} + 2OH^- \quad (1)$$

$$SiO_2 + OH^- + H_2O \rightarrow [H_3SiO_4]^- \quad (2)$$

$$AlO^{2-} + OH^- + H_2O \rightarrow [H_3AlO_4]^{2-} \quad (3)$$

$$AlO^{2-} + OH^{-} + H_2O \rightarrow [Al(OH)_6]^{3-} \quad (4)$$

$$CaSO_4 \rightarrow Ca^{2+} + SO_4^{2-} \quad (5)$$

$$2[Al(OH)_6]^{3-} + 6Ca^{2+} + 3SO_4^{2-} + 26H_2O \rightarrow CaO \cdot Al_2O_3 \cdot 3CaSO_4 \cdot 32H_2O \quad (6)$$

$$[H_3SiO_4]^{-} + [H_3AlO_4]^{2-} + Ca^{2+} \rightarrow C-(A)-S-H \quad (7)$$

3.4 Heavy metal content and leaching toxicity of solidified soil

Table 5 lists the contents of arsenic, cadmium, chromium, copper, mercury, nickel, lead and other heavy metals in group A-4 samples. The table also outlines the regulatory classifications of the soil based on GB 36600-2018'Soil Environmental Quality Construction Land Soil Pollution Risk Control Standard'. Analysis of the data reveals that the heavy metal concentrations in the solidified soil fall below the limits stipulated for first-type land use in soil environmental quality construction areas. Consequently, the flow solidified soil, produced using ammonia alkali white mud, is deemed suitable for utilization as filling material in construction engineering projects, posing negligible risks to human health.

Table 6 presents the concentrations of various heavy metals, including arsenic, cadmium, chromium, copper, mercury, nickel, lead, and others, in the leaching solution of group A-4 samples following 28 days of solidification. Additionally, it juxtaposes these concentrations with the emission concentration limits of corresponding heavy metals outlined in GB 8978-1996'Integrated Wastewater Discharge Standard' for comparison. Analysis of the data reveals that, apart from arsenic, chromium, and copper, the leaching solution of the solidified soil does not contain other heavy metal elements. Furthermore, the mass concentrations of arsenic, chromium, and copper in the leaching solution are significantly lower than the standard limits prescribed by GB 8978-1996. This indicates that the solidified soil lacks the risk characteristics associated with leaching toxicity and poses no threat of environmental pollution.

4 Conclusion

(1) The main phase composition of salt mud and white mud includes calcium carbonate, calcium sulfate, magnesium hydroxide, calcium hydroxide, sodium chloride, and calcium chloride. The characteristic particle size (d90) values of salt mud and white mud are 56.661 μm and 29.677 μm, respectively. The pore structure of white mud is more developed than that of salt mud, contributing to its relatively higher water content.

(2) With the increase of salt mud content, the fluidity of fluid solidified soil gradually increases, while the compressive strength initially rises and then declines. When the ratio of white mud to salt mud is 1:1, the fluidity of the prepared fluid solidified soil measures 176 mm, with corresponding compressive strengths of 1.07 MPa at 3 days, 3.38 MPa at 7 days, and 3.98 MPa at 28 days.

(3) The hydration products of the fluid solidified soil primarily comprise AFt and C-S-H gel. Particles such as calcium carbonate in the hydration product AFt and ammonia alkali white mud serve as a skeletal framework and nucleation matrix within the hardened body. The resulting C-S-H gel fills the interstitial gaps between particles, optimizing the structure of the hardened body, increasing its density, and providing strength to the fluid solidified soil.

(4) The heavy metal content and leaching toxicity of the ammonia-alkali white mud flow solidified soil are below the standard limit. As a construction engineering filling material, it poses no harm to human health and does not cause environmental pollution.

Data availability statement

The original contributions presented in the study are included in the article/Supplementary Material, further inquiries can be directed to the corresponding author.

Author contributions

SF: Formal Analysis, Writing–original draft, Writing–review and editing. ZL: Funding acquisition, Resources, Validation, Writing–original draft. GZ: Investigation, Project administration, Writing–review and editing. BZ: Funding acquisition, Validation, Writing–review and editing. YZ: Data curation, Methodology, Validation, Writing–original draft.

Funding

The author(s) declare that financial support was received for the research, authorship, and/or publication of this article. This study was funded by the Hebei Province Major Science and Technology Achievement Transformation Special Project (23283801Z).

Conflict of interest

Authors SF, GZ, and YZ were employed by Hebei Provincial Institute of Building Science and Technology Co., Ltd.

Authors ZL and BZ were employed by Tangshan Sanyou Chemical Co., Ltd.

Publisher's note

References

Bao, Y. J., Wang, N. N., Li, S. J., Wu, W. W., Chen, X. D., and Zhang, W. W. (2023). Influence of calcium carbide slag-desulfurization ash on basic properties and microscopic characteristics of fluid solidified soil. *Bull. Chin. Ceram. Soc.* 42 (12), 4449–4455. doi:10.16552/j.cnki.issn1001-1625.2023.12.020

Chen, S. H., Zhang, B., and Li, Q. C. (2022). Discussion on dechlorination of distiller waste mud and its resource utilization process. *Soda Ind.* (05), 9–11. doi:10.16554/j.cnki.issn1005-8370.2022.05.001

Du, H. H., Xu, D., Li, X., Li, J., Ni, W., Li, Y., et al. (2022). Application of molten iron desulfurization slag to replace steel slag as an alkaline component in solid waste-based cementitious materials. *J. Clean. Prod.* 377, 134353. doi:10.1016/j.jclepro.2022.134353

Du, Y. Q., Wang, X. Q., Zeng, W., Huo, Z. L., and Wei, S. (2021). Basic properties and engineering application of fluidized solidified soil used in road engineering. *Tianjin Constr. Sci. Technol.* 31 (03), 12–15.

Gong, X. L., Wang, Y. Z., and Chen, T. (2023). Strength model of soda residue soil considering consolidation stress and structural influence. *J. Ocean Univ. China* 22 (5), 1216–1226. doi:10.1007/s11802-023-5307-0

He, G. P. (2023). Construction technology for fertilizer backfilling of premixed fluidized solidified soil. *Archit. Technol.* 54 (16), 2031–2033.

Liao, Y. J., Yang, Q. S., and Wang, Y. J. (2012). Application research of white mud in660 MW unit FGD system. *Adv. Mech. Eng.* 524-527, 940–944. doi:10.4028/scientific.net/amr.524-527.940

Liu, C. (2021). Study on improving the filtration performance of white waste mud in solvay soda plant. *Soda Ind.* (05), 12–14. doi:10.16554/j.cnki.issn1005-8370.2021.05.003

Pan, D. W., and Xu, R. K. (2017). Research on the use of ammonia alkali waste residue as a soil amendment. *Soda Ind.* (04), 16–19. doi:10.16554/j.cnki.issn1005-8370.2017.04.004

Peng, T. C., and Liu, Z. Y. (1999). Study on desulphur of wet smoke dust using sodalime. *J. Tianjin Univ. Technol.* (S1), 57–59.

Rui, Y., Liang, Y., and Wang, Y. (2006). Wet simulation flue gas desulfurisation with soda-ash dregs absorbent. *Environ. Sci.Technol.* 29, 21–25. doi:10.19672/j.cnki.1003-6504.2006.07.009

Sun, C. Y., Zhang, J., Yan, C. W., Yin, L., Wang, X., and Liu, S. (2022). Hydration characteristics of low carbon cementitious materials with multiple solid wastes. *Constr. Build. Mater.* 322, 126366. doi:10.1016/j.conbuildmat.2022.126366

Su, Y., Yan, N., Bai, X. Y., Fu, L., Zhang, Q. J., Liang, B., et al. (2024). Research progress and application on engineering characteristics of ready-mixed fluid solidified soil. *Mater. Rep.* 1-11. http://kns.cnki.net/kcms/detail/50.1078.tb.20240116.1510.030.html.

Wang, C. C., Liu, M. Q., Song, H. Q., Geng, L. M., and Du, H. X. (2023). Experimental study on properties of red mud, steel slag powder and cement solidified fluidized soil. *Bull. Chin. Ceram. Soc.* 42 (07), 2488–2496. doi:10.16552/j.cnki.issn1001-1625.2023.07.006

Wang, S. J., Bu, H., Chen, H. J., Hu, T., Chen, W. Z., Wu, J. H., et al. (2020). Floatable magnetic aerogel based on alkaline residue used for the convenient removal of heavy metals from wastewater. *Chem. Eng. J.* 399, 125760. doi:10.1016/j.cej.2020.125760

Xu, D., Fu, P. F., Ni, W., Wang, Q., and Li, K. (2021). Characterization and hydration mechanism of ammonia soda residue and portland cement composite cementitious material. *Materials* 14 (17), 4794. doi:10.3390/ma14174794

Xu, D., Ni, W., Wang, Q. H., et al. (2020). Preparation of clinker-free concrete by using soda residue composite cementitious material. *J. Harbin Inst. Technol.* 52 (08), 151–160.

Yan, C. (2008). *Research on method of synthesisenvironment estimation and mechanism ofstrength for pure alkali residue*. Tianjin, China: Tianjin University.

Ye, Q. (2023). Research on key technologies for backfilling of flow state solidified soil on the side of trenches in coastal areas. *Constr. Saf.* 38 (06), 86–88.

Zhang, W., Hao, X. S., Wei, C., Liu, X. M., and Zhang, Z. Q. (2022). Activation of low-activity calcium silicate in converter steelmaking slag based on synergy of multiple solid wastes in cementitious material. *Constr. Build. Mater.*, 351. doi:10.1016/J.CONBUILDMAT.2022.128925

Zhang, Z., Zhu, Y., Yang, T., Li, L., Zhu, H., and Wang, H. (2017). Conversion of localindustrial wastes into greener cement through geopolymertechnology: a case study of high-magnesium nickel slag. *J. Clean. Prod.* 141, 463–471. doi:10.1016/j.jclepro.2016.09.147

Zhao, L. B., Xu, B., Li, G. F., and Zhang, J. R. (2017). Development status in comprehensive utilization of alkaline residues. *Industrial Minerals Process.* 46 (06), 73–76. doi:10.16283/j.cnki.hgkwyjg.2017.06.020

Zhao, X., Liu, C., Wang, L., Zuo, L., Zhu, Q., and Ma, W. (2019). Physical and mechanical properties and micro characteristics of fly ash-based geopolymers incorporating soda residue. *Cem. Concr. Compos.* 98, 125–136. doi:10.1016/j.cemconcomp.2019.02.009

Zhnag, L., Guo, L. J., Xu, W. Y., and Wei, X. M. (2023). Research on crucial technological and material issues of applying fine tailings to mine filling: a review. *Mater. Rep.* 37 (23), 106–116.

Zhong, W. J., Zhao, Y. W., Chen, X. M., Zhang, N., Han, L. B., Miu, H. K., et al. (2023). Effect of slag composite firming agent on mechanical strength of ready-mixed fluid stabilized soil. *New Build. Mater.* 50 (03), 46–50.

Zhou, Y. X., Huo, M. H., Hou, L., Chen, Z. D., and Zhang, L. S. (2024). Current research and prospect of low strength flowable filling materials. *Mater. Rep.* 1-16. http://kns.cnki.net/kcms/detail/50.1078.TB.20230801.1604.008.html.

Zhu, C. F., Tan, H. B., Du, C., Wang, J., Deng, X., Zheng, Z., et al. (2023). Enhancement of ultra-fine slag on compressive strength of solid waste-based cementitious materials: towards low carbon emissions. *J. Build. Eng.* 63 (PA), 105475. doi:10.1016/j.jobe.2022.105475